The 9th European Congress on Computational Methods in Applied Sciences and Engineering
ECCOMAS Congress 2024
3–7 June 2024, Lisboa, Portugal

NUMERICAL ANALYSIS OF A LARGE SCALE DISTRIBUTED PROPULSION EXPERIMENT AT HIGH LIFT

J. Oldeweme[1], M. Kamphues[1], T. K. Lindner[2], C. Bode[1], P. Scholz[2] and J. Friedrichs[1]

[1] Institute for Jet Propulsion and Turbomachinery, Technische Universität Braunschweig, Hermann-Blenk-Str. 37, 38108, jonas.oldeweme@.tu-braunschweig.de

[2] Institute for Fluid Mechanics, Technische Universität Braunschweig, Braunschweig, Hermann-Blenk-Str. 37, 38108, t.lindner@tu-braunschweig.de

Key words: Distributed Propulsion, Actuator Disc, High-Lift, URANS

Summary. Distributed propulsion configurations are a promising concept for future aircraft systems, promising a significant increase in overall aircraft efficiency and thus a reduction in emissions. In doing so, distributed propulsion configurations offer an enlarged design space. A major challenge is the unsteady propeller-propeller and propeller-wing interactions. To investigate this in more detail, such a DP configuration at high lift has been experimentally tested in previous studies. The wind tunnel model consists of a two element wing $c = 0.8\ m$ with three co-rotating propulsion units with a diameter of $D_{prop} = 0.6$ m.

The focus of this work is to further exploit the experimental data using numerical methods of different complexity of the propeller (Actuator Disc, steady-state RANS and unsteady RANS). The aim is to provide an evaluation of a well-founded and reliable qualitative and quantitative prediction of the distributed propulsion configurations. Isolated propeller simulations, including low-order BEMT and CFD calculations, were performed. While CFD results for thrust and power coefficients align well with experimental data, BEMT overestimates them. This is significant as BEMT data is also used as input in actuator disc calculations. The distributed propulsion setup was numerically analysed, showing how experimental drive strut-system affects results based on propeller position relative to the wing. Although trends like positioning are reproduced, the absence of wind tunnel walls in the numerical setup means the results aren't directly comparable to experiments. Finally, an unsteady distributed propulsion model with fully resolved propellers showed that blade loading is well captured in RANS compared to URANS, with global parameters like lift also predicted accurately. Further studies are needed to address local effects at different operating points that RANS can not model.

1 INTRODUCTION

Several aircraft concepts are currently being investigated to reduce aircraft engine emissions. Distributed Electric Propulsion (DEP) is a promising concept for future aircraft engines that requires further investigation. By increasing the number of propulsion units along the wing and by strategically placing them, conventional concepts can be outperformed [1]. Numerical studies have been carried out for different configurations and operating points. While positioning the

propeller above the wing appears to be advantageous for cruise [2], Beckers et al. show that positioning it below the wing improves performance at high-lift conditions. Here, Beckers et al. show different numerical methods to simulate unsteady effects. Bongen et al. further analyse differences between simulations in wind tunnel environments compared to free flight conditions. At high global angles of attack, the separation caused by the wind tunnel walls also affects the centre of the wing and therefore the lift. Slats near the walls can reduce this effect.

In previous studies experimental data was obtained for a distributed propulsion setup [6, 7]. In particular, important findings on the propeller-wing interaction in different positions were produced. For both wing and propeller, the position of the propeller relative to the wing is a crucial parameter. In this study, this experimental setup is analysed in more detail numerically. One focus will be on the extent to which the propeller strut-system has an influence on the performance of the setup.

2 EXPERIMENTAL SETUP

This numerical work is based on a distributed propulsion experiment, which is outlined below. Since the focus of this study is the numerical analysis of the setup, only the key features of the experimental setup are presented here. Details of the design can be found in Oldeweme [8].

In the 2.4m $\times$ 2.4m test section of the Propulsor Test Facility (PTF) of TU Braunschweig, a $b_{full} = 2.4$ m wide wing and three propeller drives are installed across the span. The setup is shown in figure 1.

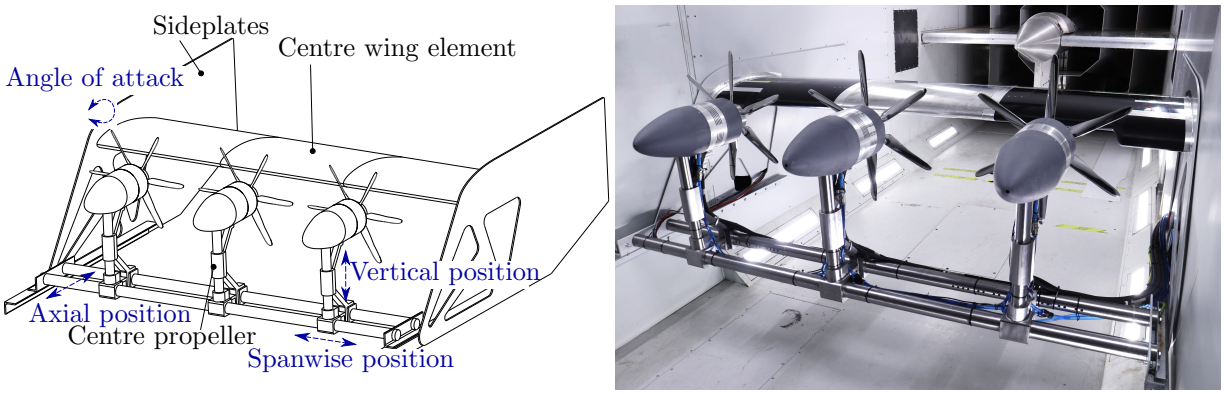

Figure 1: Test setup sketch (left) and installed in the Propulsion Test Facility (PTF) of the Institute of Jet Propulsion and Turbomachinery (right), TU Braunschweig.[6]

The wing with a chord length of $c = 0.8$ m is based on a NACA 63(2)415 airfoil, modified to include a fowler flap. It is divided into three sections, the centre section with a width of $b_{centre} = 0.7$ m is equipped with a six component balance. The centre section is mechanically decoupled from the outer sections. This creates a gap of 0.2 mm between the elements. In this way the wind tunnel effects of the side walls are reduced and periodic boundaries are created for the centre section by the outer elements. In addition to the force balance, the wing is equipped with 256 static pressure sensors along the chord at $y/c = \pm 0.35$ and along selected spanwise positions. The flap is adjustable and in this study set at an angle of $\delta = 20°$, corresponding to a take-off position. Tripping tape near the leading edge ensures fully turbulent boundary layers

on the wing and flap.

Similar to the centre wing element, the centre propeller is instrumented with a balance to measure thrust and torque. All propellers analysed in this study have an outer diameter of $D_{prop} = 0.6$ m and a hub diameter of $D_{hub} = 0.2$ m. The wing and drive trains are mounted together on side plates so that they rotate around an axis to set the angle of attack. The wing and propeller are not directly connected. This allows the forces and moments of the two central elements to be considered separately, and also allows the propellers to be positioned quickly and easily in relative to the wing. The influence of this drive train strut-system shown in figure 1 will be quantified in this numerical study. Isolated propeller simulations are also part of this work. In the experimental setup, it is possible to disassemble the two outer propellers and the entire wing in order to have an isolated measurement of the centre propeller only. Further results of the experiment can be found in Oldeweme and Lindner [6, 7, 9, 10].

3 NUMERICAL SETUP

The numerical analysis of the experimental setup is divided into three parts. Firstly, the performance of an isolated propeller is analysed. Secondly, the distributed propulsion setup is modelled. At the beginning, a steady-state Reynolds-averaged Navier-Stokes (RANS) simulation is performed using the actuator disc. In the final step, the actuator disc is replaced by a fully resolved propeller and the flow field is resolved unsteady. The DLR TAU code is used for all simulations [11]. The Spalart-Allmaras turbulence model is used for fully turbulent simulations [12].

Isolated Propeller

Part of this study is to evaluate the isolated propeller results. On the one hand, it will be compared how well a periodic CFD RANS setup reproduces the experimental results. Based on these results, detailed analyses for the design of new blades can be performed in the future. On the other hand, the blades will be recalculated using the Blade Element Momentum Theory (BEMT). An existing BEMT tool will be used for this purpose. Details of the workflow can be found in Lück [13] and Lieder [14]. For the radial blade sections selected there, 2D polars are calculated using XFOIL. These serve also as input for later simulations using the actuator disc.

In order to evaluate the results of the BEMT, and thus the input of the actuator disc, they are compared not only with the experiment, but also with isolated stationary CFD calculations. The domain from figure 2 (left) is used for this purpose. The fluid enters the domain at the inlet, which is 10 propeller radii upstream of the blade. While the outlet is 20R downstream, the farfield is 12.5R away. As the full configuration is a six-bladed propeller, a 60° segment with a single blade in the centre and periodic boundary conditions is used here. A rotating reference frame is defined to account for the rotation of the propeller blade. The blade itself is modelled with viscous walls, while the friction of the hub is neglected by using inviscous euler walls. As can be seen on the left side of figure 2, the domain around the blade is subdivided into further regions where the mesh is significantly refined.

Distributed Propulsion

The steady-state and transient simulations of the distributed propulsion configuration are carried out in the same domain with differences of the propeller, which is shown in figure 2

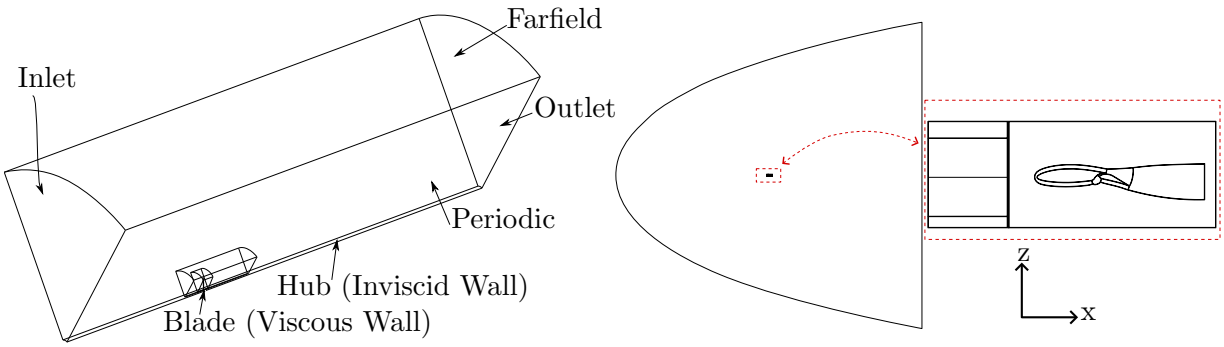

Figure 2: Computational domain of the investigations for the isolated Propeller CFD (left) and the DP-setup under free flight conditions (right).

(right). As these are performed in free flight conditions neglecting the wind tunnel walls, the periodic boundaries in the $xz-$ plane are spaced 0.7m apart in the spanwise direction (y) and thus correspond to the periodic configuration of the wind tunnel test. The magnified section in the wing area illustrates the block-structured mesh metric.

In addition to the periodic boundary conditions for the surfaces in the $xz-$ plane, the inflow and outflow (in the $x-$ direction) at the edges are defined by a farfield boundary condition and allows the specification of the inflow velocity V_∞ and the global angle of attack α. The boundaries are located in the plane shown in all directions at a distance of 100 c from the leading edge of the wing, the origin of the coordinate system. All physical walls in the model, such as the wing or the nacelle, are defined as viscous walls.

In steady-state simulations, the actuator disc model is used to simplify the effects of the propeller [15]. This allows the geometry of the propeller to be specified by the input of polars of defined radial sections and the specification of the operating point of the propeller, such as rotational speed or pitch angle. The actuator disc is replaced by a fully resolved propeller rim in the unsteady simulations. The computations are then performed in steps of 3° revolution.

One focus of this study is the influence of the propeller position. For this purpose, two positions of the experimental setup were chosen, which are listed in table 1. One is the

Table 1: Two analysed positions of propeller centre with origin in wing leading edge.

	Reference position	**Low and close position**
x/c	-0.46875	-0.1875
z/c	0	-0.2

reference position, where the propeller is horizontally far from the wing and the axis of rotation is at the same height as the leading edge of the wing. The second position is closer to the wing and the axis of rotation is below the wing. In addition to the propeller position, the influence of the propeller strut-system was analysed. For the low and close position the setups with and without the struts are shown in figure 3. Compared to the true geometry shown in figure 1, the strut-system has been simplified. In addition to the vertical strut for adjusting the relative height of the propellers, the two horizontal struts on which the propellers can be moved spanwise have been included in the setup. The diameter and position of the struts are the same as the original geometry from the experiment. Within the DP-setup the propeller has a rotational

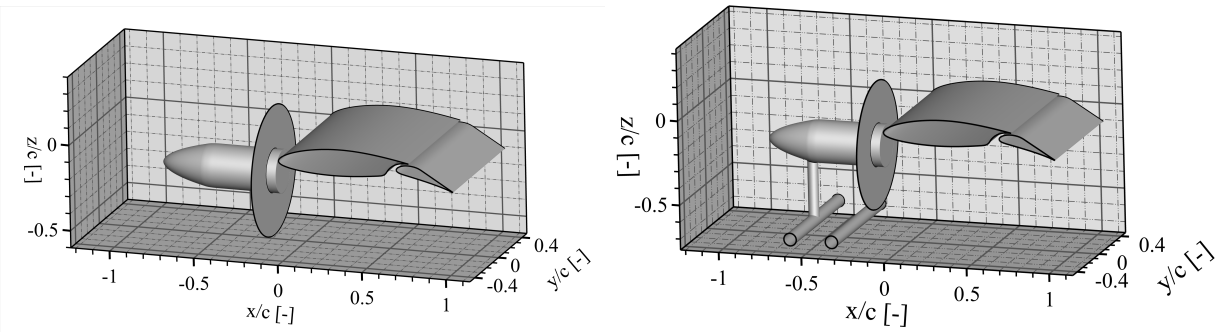

Figure 3: Geometry of the distributed propulsion configuration without (left) and with (right) strut-system shown for the low and close coupled position.

speed of $n = 6160\,\mathrm{min}^{-1}$. The freestream velocity is set to $V_\infty = 40$ m/s and the flap angle is fixed at $\delta = 20°$.

Due to the complexity of the unsteady simulations, only one position (reference position) was carried out with one defined operation point at a global angle of attack of $\alpha = 0°$, neglecting the propeller strut-system.

4 RESULTS

The same procedure as for the setups presented is followed for the results of these studies. An isolated consideration of the propeller blades is followed by steady-state and transient analyses of the distributed propulsion setup. In addition to the influence of the experimental setup, e.g. strut-system and positioning of the propeller, the focus is on the comparison between the steady-state and transient solutions.

Isolated Propeller

Figure 4 shows the thrust coefficient c_t and the power coefficient c_p for different advance ratios J.

Within the advance ratio sweep the rotational speed $n = 6050\,\mathrm{min}^{-1}$ and diameter $D_{prop} = 0.6$ m as well as the pitch angle $\beta_{Prop} = 17.25°$ remain constant, so that only the inflow velocity V_∞ is varied. The results of the experiment are compared with the numerical solutions from BEMT and CFD RANS simulation. Due to the limited power of the electric propeller motors and the maximum speed of the wind tunnel, the results are shown for the advance ratio between $J = 0.5$ and $J = 1$. For both, the thrust and power coefficients, the CFD results are in good agreement with the experimental data. The simulations slightly overestimate the results for both coefficients. The BEMT, on the other hand, significantly over predicts the results. Furthermore, the slopes of the two coefficients are different. The incorrect prediction of the data is mainly due to the polars used, which are only from a 2D solver. The polars therefore neglect rotational effects that act on the individual sections depending on the radial position. Further studies should investigate this influence with the geometries used [16].

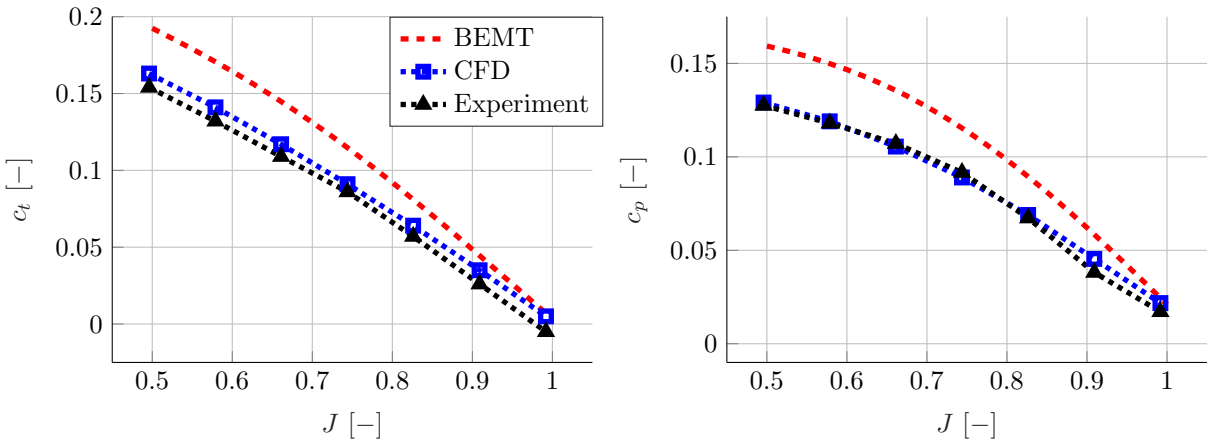

Figure 4: Thrust and power performance map of the isolated propeller

Distributed Propulsion

For the steady-state simulations, the presented setups are used with and without the struts as well as two different propeller positions relative to the wing of table 1. Figure 5 shows the top view of the both setups with a global angle of attack of $\alpha = 8°$. In addition to the schematic representation of the propeller position, the wing including flap can be seen. On the left, without the strut-system of the propeller drive from the experiment and on the right with it.

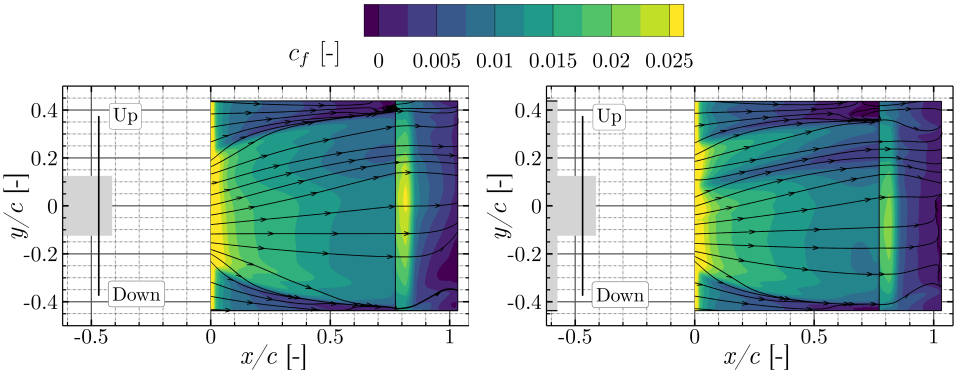

Figure 5: Surface solution for the friction coefficient with plotted streamlines for a configuration without (left) or with the strut-system (right) in the reference position at $\alpha = 8°$.

In both simulations, the propeller thrust was adjusted to the experimental thrust at the beginning of the angle of attack sweep ($\alpha = 0°$). This was done to create a comparable flow field. The suction side of the wing shows the friction coefficient c_f. Looking first at the configuration without the strut-system, a complex but almost undisturbed and separation free flow field on the main wing and flap is emerged. Separation areas can be identified by friction coefficients smaller than zero. In the periodic configuration, these only occur very isolated at the end of the main wing in the gap between the propeller wakes on the upwash side at $[x/c = 0.75,\ y/c = 0.4]$,

as well as in the rear area of the flap on the downwash side at $[x/c = 1,\ y/c = -0.26]$. The numerical simulation thus confirms the experimental separation behaviour observed by Lindner [7]. Furthermore, the non-symmetric cross-flow in a periodic configuration with distributed drives can be visualised. The course of the streamlines in the direction of the upwash side, both from the centre of the wing and from the periodic boundaries, can be clearly seen. This is due to two overlapping effects: Firstly, the higher load on the propeller on the downwash side results in an increased mass flow which spreads towards the less loaded side (upwash). Secondly, the effective angle of attack on the upwash side is increased by the additional upward component of the local flow, which also increases the lift or negative pressure. This pressure gradient in the spanwise direction increases the crossflow to the upwash side. Contrast this with the configuration with the struts on the right side of figure 5 where a significant difference can be seen. The wake from the vertical strut, indicated by the low level of the friction coefficient contour, intersects the main wing element and extends across the entire wingspan. The destabilising effect increases the separation area at $[x/c = 0.75,\ y/c = 0.4]$.

In a following step, the relative position of the propeller to the wing is shifted. The propeller is now closer to the wing and its axis of rotation is below the leading edge of the wing. The results of the suction side of the wing at an angle of attack of $\alpha = 10°$ are shown in figure 6. This shows a much more complex flow pattern for close and low position than for the first

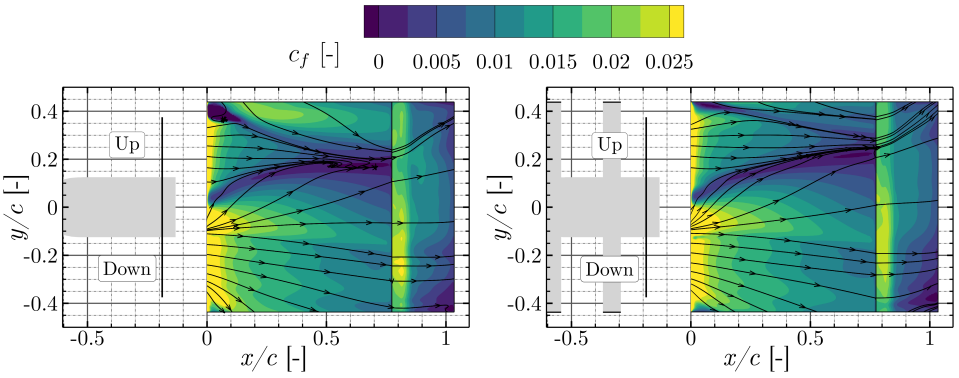

Figure 6: Surface solution for the friction coefficient with plotted streamlines for a configuration without (left) or with the strut-system (right) in the low and close position at $\alpha = 10°$.

reference position. A distinct wake can be seen extending from the centre of the leading edge over the upwash side to the trailing edge of the main wing for both, without (left) and with (right) the strut-system. The resulting zone of low coefficient of friction is almost identical for both configurations and is therefore not due to the vertical strut. In addition, a second flow disturbance occurs near the periodic edge on the upwash side. A possible reason for this is the stronger cross-flow without struts due to the different load on the actuator disc. The flow pattern at the flap is unaffected by the strut-system.

A slice through the centre plane at $y/c = 0$ in figure 7 shows that the nacelle, and not the strut-system, is causing this flow pattern. The nacelle wake is unaffected by the struts and impinges on the leading edge of the main element in both configurations. Following the streamlines around the horizontal strut, the disturbed flow does not hit the flap, unlike the first reference position, which explains the identical flow field there.

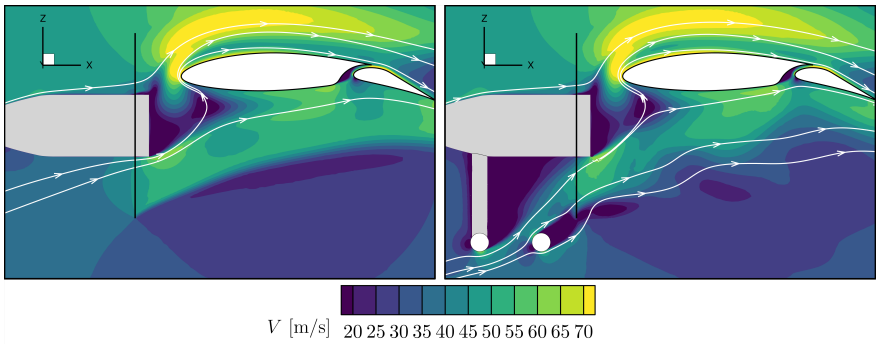

Figure 7: Flow field and wakes of the configuration without and with struts in the low and close position $\alpha = 10°$. Section through the centre plane at $y/c = 0$.

Figure 8 shows the lift polars of the wing in the first reference position (left) and for the low and close position (right) for both configurations and compares that with data from the experiment. No wind tunnel correction of the experimental data have been done yet.

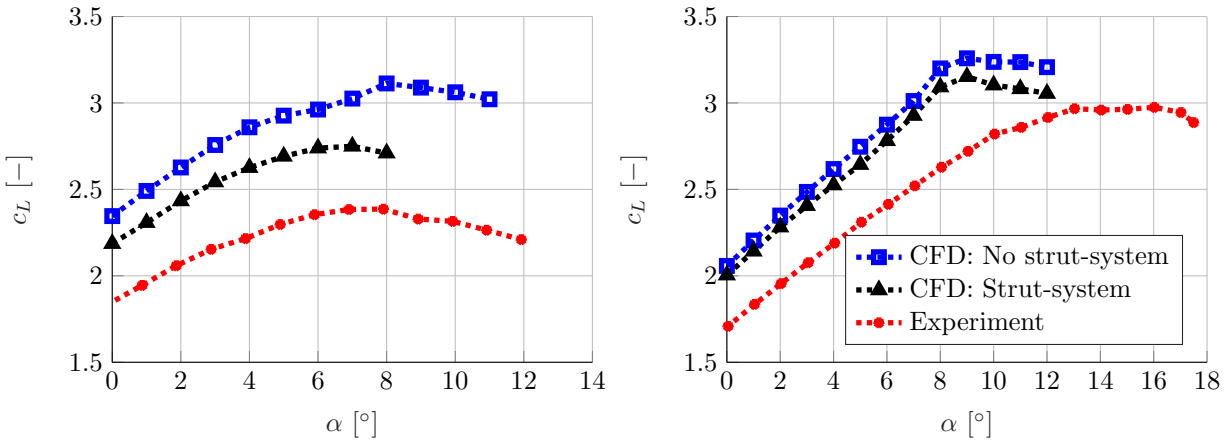

Figure 8: Comparison of numerical (with and without the strut-system) and experimental lift polars at reference position (left) and low and close position (right).

Starting with the reference position, at higher angles of attack, i.e. in the range of maximum lift, there are significant differences. Without the strut-system, the wing reaches a $c_{L,\max} \approx 3.03$ at an angle of attack of $\alpha = 8°$. In addition, the high lift coefficient can be maintained over a wider range of angles of attack before the flow stalls completely. When the strut-system is taken into account, the stall occurs a little earlier and more abruptly. The maximum lift coefficient there is $c_{L,\max} \approx 2.75$, for an angle of attack of $\alpha = 7°$. The losses in maximum lift are therefore $\Delta c_{L,\max} = -0.28$, which corresponds to a relative deviation of -9.2%.

The effect of the strut-system on lift is also investigated for the low and close position on the right side of figure 8. Due to the lower and closer position of the propeller, it is expected that the wake of the vertical strut will not hit the main element of the wing as seen before and will therefore have less influence on the overall behaviour of the wing. Contrary to the reference

position, there is no significant difference in the behaviour at the polars. In terms of lift, the configuration with struts is below the configuration without struts with an almost constant offset of $\Delta c_L \approx -0.1$ for all angles of attack. Both simulations reach their maximum lift coefficient $c_{L,\max}$ at $\alpha = 9°$, slightly later than the reference position.

In both positions the two configurations with and without the strut-system do not match well with the experimental data. The simulations performed here were carried out under free flight conditions using the centre propeller and wing segment with periodic boundaries. Due to the lack of a wind tunnel environment and the resulting change in the effective angle of attack, they differ from the experimental results. For the reference position, a setup was also simulated with wind tunnel environment but without the propeller drive strut-system. In this case the full width of the wing was considered with three wing segments and three actuator discs. With a global angle of attack of $\alpha = 0°$, a lift of $c_L = 2.14$ was achieved at the centre wing segment. This is approximately the same as the strut-system simulation. Although not part of this work, further studies will be carried out for both positions and with the drive strut-system at selected angles of attacks.

Unsteady Simulations

Finally, the results of the unsteady simulations are compared with those of the steady-state simulations and the experiment. Some key values are shown in table 2. The pitch angle of the numerical fully resolved propeller blades corresponds to the angle of the experiment with $\beta_{Prop} = 17.25°$. The simulations of the stationary actuator disc simulations used in this chapter have been adjusted to change the pitch angle so that the thrust generated matches with the URANS. As shown in the first part of the results, the polars used for the actuator disc overestimate the thrust generated. In order to obtain a comparable flow field, the actuator disc is pitched down to $\beta_{Prop} = 15.56°$, so that the thrusts of both numerical methods are about $T = 194.5$ N and thus about 10 N below the experimental values.

Table 2: Integral values of numerical and experimental data in reference position at $\alpha = 0°$.

	URANS	**Actuator Disc**	**Experiment**
β_{Prop}	17.25°	15.56°	17.25°
Thrust	194.5 N	194.4 N	204.6 N
c_L	2.193	2.294	1.845

Figure 9 shows the surface blade loading in the direction of flow for the fully resolved propeller (left) and the load on the actuator disc of the simplified, steady-state simulation with identical thrust. For the comparison between the unsteady simulation and the actuator disc, the data is generated by discrete radial sections of $\Delta\theta = 3°$ in order to use the same methodology between the two approaches. For both the actuator disc and the resolved propeller, the additional load on the down going blade is clearly visible. Both approaches show a local maximum near the nacelle. The simplified approach of the actuator disc reflects the non-symmetric thrust behaviour with good accuracy, although the additional load at the maximum is overestimated both in terms of magnitude and local concentration. In order to achieve identical thrusts, the actuator disc has significantly lower surface loads on the opposite side than the fully resolved propeller. This is particularly true in the region $r/R \to 1$ near the tip of the blade.

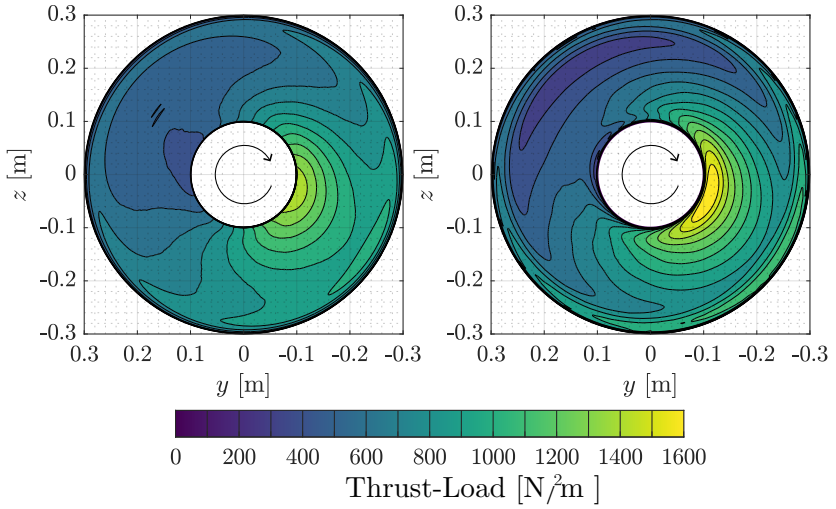

Figure 9: Comparison of the blade load of the fully resolved propeller (left) and the actuator disc (right) at the same total thrust in reference position at $\alpha = 0°$.

Lastly, table 2 shows that the wings lift is higher in the numerical solutions than in the experiment, as seen before. In order to identify the origin of the significantly higher total lift of the simulations despite lower thrusts, the experimentally measured pressure curves in the axial direction at $y/c = \pm 0.35$ are compared with the data from the numerical investigation. The pressure data is shown in figure 10. It is noticeable that the suction peak on both the upwash

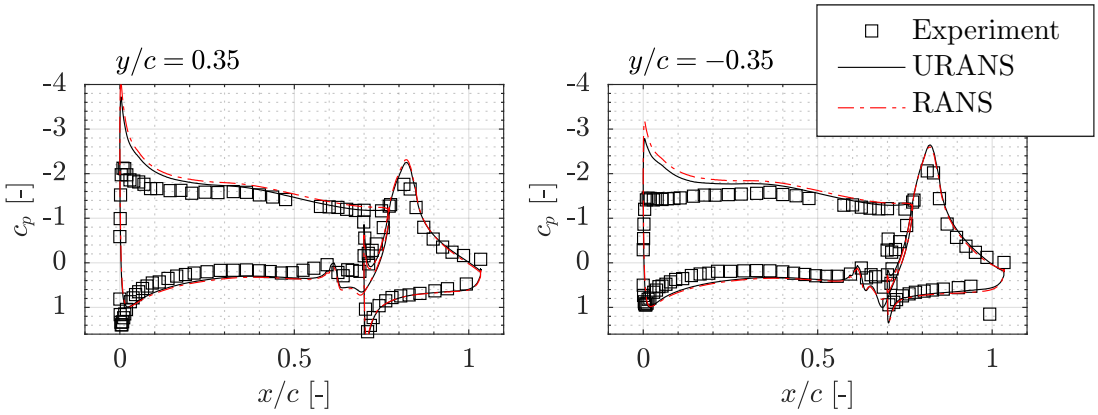

Figure 10: Pressure coefficient on the wing along the chord at $y/c = \pm 0.35$ in the propeller slipstream in reference position at $\alpha = 0°$.

($y/c = 0.35$) and the downwash side ($y/c = -0.35$) is significantly weaker or not reproduced at all compared to the experiment. As the expression of the suction peak is strongly dependent on the local angle of attack, it is reasonable to assume that it is affected by geometric influences in the wind tunnel model as shown in the steady-state results. As a result, the simulations under free flight conditions show a larger absolute pressure coefficient on the entire upper and lower profile than the experiment. The only exception is the pressure peak near the leading edge

on the underside of the wing, which is more pronounced and closer to the leading edge in the experiment. This observation indicates a different position of the stagnation point and confirms the assumption of different effective angles of attack between the experiment and the numerical model. The pressure curve on the flap is simulated with good accuracy in both simulations. This section has shown that when considering global values and the global flow field, there are only small differences between the steady-state and transient solutions. However, the steady-state solution is not able to resolve transient and local effects.

5 CONCLUSION

The presented large-scale distributed propulsion model has been numerically analysed in this work. Two numerical setups were created and studied. On the one hand, isolated propeller simulations were carried out. In addition to the low order BEMT, isolated CFD calculations were also performed. While the CFD results of the thrust and power coefficients agree well with the experimental results, the BEMT is significantly higher and overestimates the data. This finding is important because the polars used in the BEMT are also used in the actuator disc calculations of this work.

On the other hand, the distributed propulsion setup was set up numerically. The steady-state calculations show the influence of the experimental strut-system of the drives for two different positions of the propeller relative to the wing. While in the reference position the wing experiences the wake of the strut-system, the influence is comparatively smaller in the low and close positions. Here, the nacelle wake dominates. Due to the free flight environment in the numerical calculation and the associated missing wind tunnel walls, the results are not directly comparable with the experiment. While trends such as positioning can be reproduced well, the influence of the wind tunnel environment needs to be investigated in further studies.

In a final step, the distributed propulsion model has been computed unsteady with fully resolved propellers. It can be seen that the blade loading of the propeller with the actuator disc is well approximated compared to URANS. Other global parameters such as lift are also similar predicted by the unsteady and steady-state solution.

Acknowledgements

The numerical work of this paper is performed within the LuFo project InPAH, funded by the German federal ministry of economic affairs and climate action. The experimental campaign received funding from the Clean Sky 2 Joint Undertaking (JU) under grant agreement No 101007567. The JU receives support from the European Union's Horizon 2020 research and innovation programme and the Clean Sky 2 JU members other than the Union.

References

[1] Deere, K. A., Viken, S., Carter, M., Viken, J. K., Wiese, M., and Farr, N., "Computational Analysis of Powered Lift Augmentation for the LEAPTech Distributed Electric Propulsion Wing," *35th AIAA Applied Aerodynamics Conference*, American Institute of Aeronautics and Astronautics, Reston, Virginia, 2017. https://doi.org/10.2514/6.2017-3921.

[2] Kirsch, B., and Friedrichs, J., "CFD Parameter Studies Using an Actuator Disk to Quantify the Interactions on an Airfoil Segment for Distributed Propulsion," *Volume 1: Aircraft Engine*, American Society of Mechanical Engineers, 2023. https://doi.org/10.1115/gt2023-101248.

[3] Beckers, M. F., Schollenberger, M., Lutz, T., Bongen, D., Radespiel, R., Florenciano, J. L., and Funes-Sebastian, D. E., "Numerical Investigation of High-Lift Propeller Positions for a Distributed Propulsion System," *Journal of Aircraft*, Vol. 60, No. 4, 2023, pp. 995–1006. https://doi.org/10.2514/1.c037248.

[4] Beckers, M. F., Schollenberger, M., and Lutz, T., "Numerical Simulation of the Unsteady Slipstream of Lift Augmenting Distributed Propellers," 2024. https://doi.org/10.25967/610132.

[5] Bongen, D., Beckers, M. F., Schollenberger, M., Bergmann, D. P., Lutz, T., Gothow, A., Saeed, M., Weiss, J., Bardenhagen, A., and Radespiel, R., *Simulation of a Distributed Propulsion System in a Wind Tunnel*, 2022. https://doi.org/10.2514/6.2022-3818.

[6] Oldeweme, J., Lindner, T. K., Scholz, P., and Friedrichs, J., "Experimental Propeller Performance Analysis on a Large Scale Distributed Propulsion Configuration at High Lift," *International Journal of Gas Turbine, Propulsion and Power Systems*, Vol. 15, No. 1, 2024, pp. 32–39. https://doi.org/10.38036/jgpp.15.1{_}32.

[7] Lindner, T. K., Oldeweme, J., Scholz, P., and Friedrichs, J., "Experimental Propeller Placement Analysis for a Distributed Propulsion Wing Section in High Lift Configuration," *AIAA AVIATION 2023 Forum*, American Institute of Aeronautics and Astronautics, Reston, Virginia, 06122023. https://doi.org/10.2514/6.2023-3539.

[8] Oldeweme, J., Lindner, T., Scholz, P., and Friedrichs, J., "Experiment Design for a Distributed Propulsion Configuration at High Lift," DLRK, 2022. https://doi.org/10.25967/570125.

[9] Lindner, T. K., Oldeweme, J., Scholz, P., and Friedrichs, J., "System Performance of Wing and Propellers in a Periodic Distributed Propulsion Experiment," *Journal of Physics: Conference Series*, Vol. 2716, No. 1, 2024, p. 012003. https://doi.org/10.1088/1742-6596/2716/1/012003.

[10] Oldeweme, J., Lindner, T. K., Scholz, P., and Friedrichs, J., "Experimental Propeller Performance Analysis of Distributed, Single and Isolated configurations," *Journal of Physics: Conference Series*, Vol. 2716, No. 1, 2024, p. 012004. https://doi.org/10.1088/1742-6596/2716/1/012004.

[11] Schamborn, D., Gerhold, T., and Heinrich, R., "The DLR-TAU-code: Recent applications in research and industry," , 2006.

[12] Spalart, P., and Allmaras, S., "A one-equation turbulence model for aerodynamic flows," *30th Aerospace Sciences Meeting and Exhibit*, American Institute of Aeronautics and Astronautics, Reston, Virigina, 01061992, p. 523. https://doi.org/10.2514/6.1992-439.

[13] Lück, S., Göing, J., Wittmann, T., Kirsch, B., Benjamin, L., and Friedrichs, J., "Propeller design and performance evaluation with partially prescribed velocity distribution," *Proceedings of Global Power and Propulsion Society*, 2021, p. 2021.

[14] Lieder, D., Oldeweme, J., Kirsch, B., and Friedrichs, J., *Comparison of Blade Element Momentum and Lifting Line Models for preliminary Propeller Design*, 2024. https://doi.org/10.2514/6.2024-4555.

[15] Raichle, A., Stefan, M.-W., and Himisch, J., "A new Actuator Disk Model for the TAU Code and application to a sailplane with a folding engine," *STAB-Symposium 2006*, 2006. URL https://elib.dlr.de/46423/.

[16] Schollenberger, M., and Lutz, T., "Comparison of Different Methods for the Extraction of Airfoil Characteristics of Propeller Blades as Input for Propeller Models in CFD," *New Results in Numerical and Experimental Fluid Mechanics XIII*, Springer International Publishing, Cham, 2021, pp. 24–34.